AI-assisted dynamic tissue evaluation for early bowel cancer diagnosis using a vibrational capsule*

Kenneth Omokhagbo Afebu[1], Jiyuan Tian[1], Yang Liu[1], Evangelos Papatheou[1] and Shyam Prasad[2]

***Abstract*— With early sign of bowel cancer being changes in affected lesions biomechanical properties, an AI-assisted dynamic tissue evaluation is proposed for early bowel cancer diagnosis. Dynamic signals from a self-propelled vibrational capsule in contact with in-situ bowel lesions were processed and analysed for features that may be indicative of biomechanical changes in the lesions. Different combinations of the features were used to develop different lesion characterisation models. Supervised classification using Multi-Layer Perceptron (MLP) and Stacking Ensemble networks (SE) was carried out alongside unsupervised classification using K-means clustering. The SE base-learners comprised Support Vector Machine (SVM), Decision Tree, Naïve Bayes and Random Forest. Cross-validation on simulated test data showed that the SEs outperformed their composite base-learners, however, SVM as a base-learner showed tendency to yield greater than 90% accuracy. The MLPs outperformed the SEs in accuracies and in numbers of high-performance models, hence, were the only supervised network used during experimental validation and they yielded an average accuracy of 96.5%. For unsupervised classification, both simulation and experimental data showed that the lesions are best clustered into two categories representing benign and malignant lesions.**

I. Introduction

The intestinal mucosa of the human digestive tract including the small and large bowel are sometimes characterised with different lesions. Some of these lesions can mutate over time from benign (i.e. adenoma) to malignant (i.e. adenocarcinoma). Bowel lesions that have mutated to become malignant are referred to as bowel cancer. Globally, bowel cancer is the second most common cause of cancer deaths in men and women with about one million deaths per year [1], however, studies have shown that patients have 98% chance of surviving if diagnosis is made early [2]. This makes early diagnosis a crucial part of bowel cancer treatment and survival, however, most of the existing screening methods rely on post-development features including number, size and shape of polyps to infer diagnosis [3]. With these methods, advanced stage bowel cancer are easily detected but the early stage bowel cancer are quite difficult to detect as they often appear as subtle mucosal lesions [4]. A more recent screening method is the non-invasive capsule endoscopy which makes use of a wireless pill sized video camera to examine the inside of the bowel [5]. Capsule endoscopy was developed to meet the increasing demand for bowel cancer screening while reducing the discomfort, risk of infection, manoeuvring difficulty and vigorous training often associated with conventional colonoscopy [6], [7].

Like other cancers, the development of bowel cancer often start with changes in biomechanical properties [8] of affected lesions and this is often obscured and unquantifiable to the endoscopist, thus making early detection very difficult. In this study, a non-invasive biomechanical evaluation of lesions is carried out using readily measurable dynamics of a self-propelled capsule and machine learning. The resulting dynamics of the capsule travelling and encountering lesions in the bowel are envisaged to carry information that are intrinsic to encountered lesions. The measured dynamics are processed and analysed for features that may be indicative of biomechanical differences in the lesions. With no established relationship between the resulting features and the lesion's biomechanical properties, machine learning algorithms capable of learning complex relationships from data were adopted for classifying the features into different biomechanical classes. Supervised classification using Multi-Layer Perceptron (MLP) and Stacking Ensemble networks (SE) was carried out alongside unsupervised classification using K-means clustering. During supervised learning, the algorithms were first trained to find patterns from a large dataset and the trained models were later used to make prediction on unseen data. For unsupervised learning, attempt was made at classifying all the data into desired classes without prior training.

Stiffness is one of the measurable biomechanical properties that tends to increase at the early stage of bowel cancer development [8], [9]. This is suggested to be as a result of the overproduction of collagens, alignment of fibres and pathological collagen crosslinking [8]. As a measure of resistance to deformation, tissue stiffness has often been denoted as Young's modulus in most literature with stiffer materials having higher values. Studies such as [9], [10] have demonstrated how biomechanical characterisation can be used to distinguish between healthy and cancer infected tissues. However, these previous biomechanical characterisation have always required invasive retrieval of the tissues via surgery or biopsy, but in this present study a non-invasive method is introduced. The schematic illustration of the proposed early bowel cancer detection is presented in Fig. 1 and this novel approach is expected to make early stage bowel cancer detection possible and easier.

The remaining of this letter is structured as follows. Section II introduces the mathematics, operational modes and

*This work was supported by the EPSRC under Grant No. EP/V047868/1.

[1]K. O. Afebu, J. Tian, Y. Liu and E. Papatheou are with Engineering Department, University of Exeter, Exeter EX4 4QF, UK. k.afebu,jt535,y.liu2,e.papatheou@exeter.ac.uk

[2]S. Prasad is with Endoscopy Department, Royal Devon University Healthcare NHS Foundation Trust, Barrack Road, Exeter, EX2 5DW, UK. shyamprasad@nhs.net

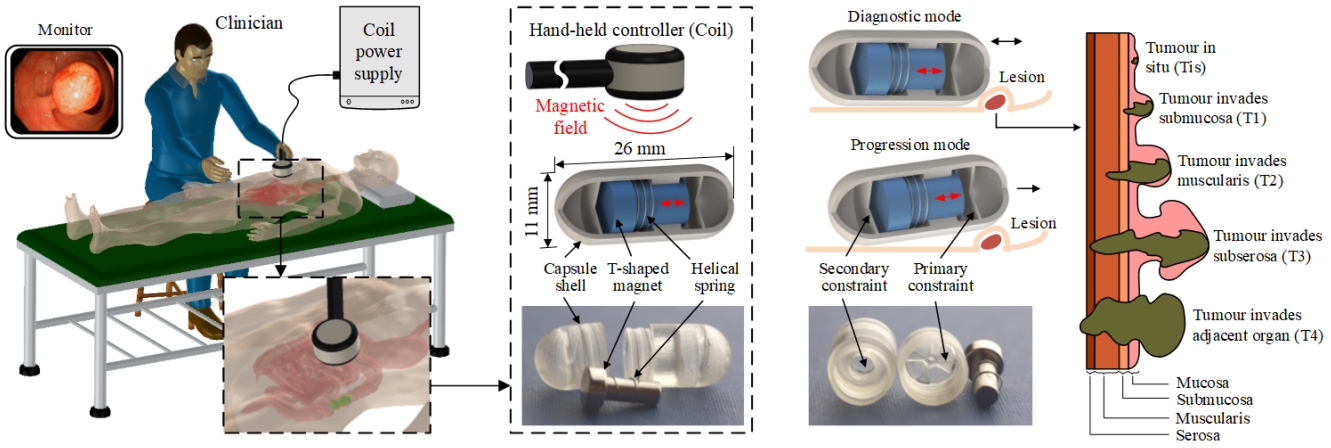

Fig. 1. Conceptual design and real-world prototype of the vibrational capsule system for early bowel cancer detection, where a capsule prototype, 26 mm in length and 11 mm in diameter, was fabricated. The prototype contains a T-shaped permanent magnet for vibration, a helical spring for reverting the magnet's position and a capsule shell with a primary and a secondary constraint for restricting the vibration of the magnet. Once the magnet is excited by the external electromagnetic field using a square wave signal, it may impact with the constraints, so the capsule can progress either forward or backward. During the procedure, a clinician will hold a coil panel above the capsule to guide it from the patient's rectum to the cecum. The capsule has two operational modes: progression and diagnostic. In progression mode, the capsule is driven to the place of interest, while in diagnostic mode, it is stabilised at a location where a lesion is detected for further diagnosis. In progression mode, responses favourable for the capsule's progression are most likely until a lesion is encountered. In diagnostic mode, the capsule's responses are determined by the bowel tissue's biomechanical properties, such as mucosal friction and encountered lesion's elastic modulus.

accompanying dynamics of the capsule. Measurable dynamic signals and extractable features are described in Section III while the machine learning algorithms used for the AI models are discussed in Section IV. The results of the training and testing of the AI models are presented in Section V for both simulation and experimental data. The letter is rounded-off with some discussions and conclusions in Section VI.

II. The Self-Propelled Vibrational Capsule

The self-propelled vibrational capsule was invented to reduce the long hours of capsule endoscopic procedures while also permitting forward and backward motion control, allowing endoscopists to re-visit areas of interest.

A. Mathematical model

The capsule shown in Fig. 2 has a cylindrical body of length L, radius of R and mass m_c with a bowel lesion of height h_p and width w_p in front. It is driven by an externally excited magnetic inner mass m_m impacting a secondary and a tertiary spring constraint with stiffnesses k_1 and k_2, respectively. As seen from the figure, a primary damping spring with stiffness k and damping c connects m_m to the capsule shell. k_1 and k_2 are separated from m_m by gaps g_1 and g_2, respectively. The inner mass is subjected to periodic excitations using an external periodic force F_e, in this case a square waveform signal given as

$$F_e = \begin{cases} P_d, & \text{mod } (t,T) \in [0, DT], \\ 0, & \text{otherwise}, \end{cases} \tag{1}$$

where P_d, T and $D \in [0, 1]$ represent the amplitude, period, and duty cycle ratio of the excitation force, respectively and mod (t, T) indicates t modulo T.

By impacting the forward and backward constraints, the inner mass drives the capsule either forward or backward.

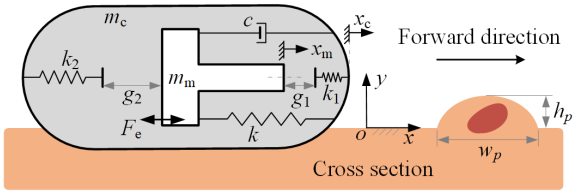

Fig. 2. Physical model of the vibrational capsule with a bowel lesion.

Considering the free-body diagram and the prevailing forces, the dynamics of the capsule's motion in the bowel can be modelled as [11],

$$\begin{cases} m_m \ddot{x}_m = F_e - F_i, \\ m_c \ddot{x}_c = F_i + F_x + F_f, \end{cases} \tag{2}$$

where F_i is the interactive driving force impacted on the capsule by the inner mass represented as

$$F_i = \begin{cases} kx_r + cv_r + k_1(x_r - g_1), & \text{if } x_r > g_1, \\ kx_r + cv_r, & \text{if } -g_2 \leqslant x_r \leqslant g_1, \\ kx_r + cv_r + k_2(x_r - g_2), & \text{if } x_r < -g_2. \end{cases} \tag{3}$$

Here $x_r = x_m - x_c$ and $v_r = \dot{x}_m - \dot{x}_c$ respectively represent the relative displacement and velocity between the inner mass and the capsule shell. On the other hand, F_x and F_f respectively represent the horizontal reaction from the lesion and the Coulomb friction that accounts for tangential contact forces, where the vertical force F_y from the lesion cancels the capsule gravity G. Depending on these two forces, the overall frictional force is given as

$$F_f = \begin{cases} -\text{sign}(\dot{x}_c)\mu G, & \text{if } \dot{x}_c \neq 0 \\ -\text{sign}(F_i + F_x)\mu G, & \text{if } \dot{x}_c = 0 \text{ and } |F_i + F_x| \geq \mu G \\ -F_i - F_x, & \text{if } \dot{x}_c = 0 \text{ and } |F_i + F_x| < \mu G \end{cases} \tag{4}$$

where μ is the frictional coefficient and F_f has been proven to sufficiently represent the friction between the intestinal

walls and the capsule [12]. For a detailed study of F_x, readers can refer to [11].

B. Dynamics of the vibrational capsule

Excitation amplitude, period and duty cycle are the capsule parameters that are alternated to drive and impose the different operational modes on the capsule. This can either be the diagnostic or progression modes (Fig. 1). In diagnostic mode, the inner mass is restricted to forward impacts that causes the capsule to move but sticks and vibrates on lesions. During progression, the capsule is made to either move forward or backward via impacts of the inner mass with the forward or backward constraint, respectively. These capsule modes alongside their representative dynamical variables and phase portraits are illustrated in Fig. 3. For $(D, T) = (0.2, 0.05)$, $(0.2, 0.07)$ and $(0.3, 0.05)$, diagnostic modes were observed for $P_d \in [25, 40]$ mN, $[20, 29]$ mN and $[20, 29]$ mN, respectively. The vibro-impacts imposed on the capsule are well obvious from the inner mass acceleration signals ($\ddot{x}_m$), and it is seen to relatively exhibit either the period-one motion with one impact per period of excitation or the period-two motion with two impacts.

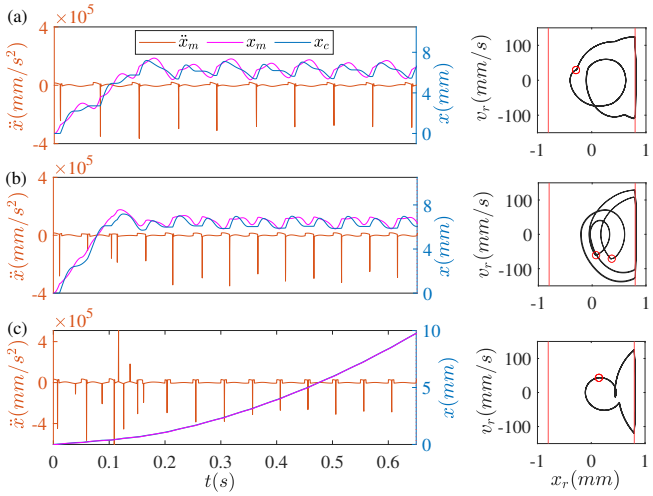

Fig. 3. Measurable dynamics of the capsule and their phase trajectories for (a) period-one motion with one impact per period of excitation (diagnostic mode) (b) period-two motion with two impacts (diagnostic mode) and (c) period-one motion with one impact (progression mode). Red, pink and blue lines on the left panels represent the acceleration ($\ddot{x}_m$) and displacement (x_m) of the inner mass and the capsule's displacement (x_c), respectively. Black, vertical red lines and red circles on the right panels denote the capsule's phase trajectories on the (x_r, v_r) plane, impact boundaries of the constraints and the Poincaré sections of the trajectories, respectively.

III. Capsule Signals and Feature Extraction

With respect to the works of Yan *et al.* [11], the dynamics of the capsule encountering a conical intestinal lesion (see Fig. 2) were simulated for parameters given in Table I. The investigated tissue stiffness varied in $E \in [12, 170]$ KPa and were labelled into five classes as shown in Table II. $E \in [2, 70]$ kPa, stiffness values were sampled at a step size of 1.2 kPa, while for $E \in [72, 170]$ kPa, they were sampled at 2.4 kPa. In all, 2363 dynamical signals of capsule's displacement x_c were generated in the diagnostic mode. White Gaussian noise of signal-to-noise ratio 20 was added to the simulated signals before smoothening as exemplified in Fig. 4 in order to adapt them to experimental scenarios.

TABLE I
Capsule Parameters for the Dynamic Simulation.

Parameters	Symbols	Units	Values
Capsule length	L	mm	26
Capsule radius	R	mm	5.5
Capsule mass	m_c	kg	0.00167
Inner mass	m_m	kg	0.0018
Primary stiffness	k	N/m	62
Secondary stiffness	k_1	N/m	27900
Tertiary stiffness	k_2	N/m	53500
Gap to k_1	g_1	mm	0.8
Gap to k_2	g_2	mm	0.8
Damping	c	Ns/m	0.0156
Duty cycle ratio	D	-	[0.2,0.3]
Excitation period	T	s	[0.05,0.07]
Lesion height	h_p	mm	8
Lesion width	w_p	mm	8

TABLE II
Investigated E-values and Affixed Class Labels.

E-values (kPa)	Class label
$E \leqslant 39.6$	$E0$
$39.6 < E \leqslant 67.2$	$E1$
$67.2 < E \leqslant 98.4$	$E2$
$98.4 < E \leqslant 129.6$	$E3$
$129.6 < E \leqslant 170$	$E4$

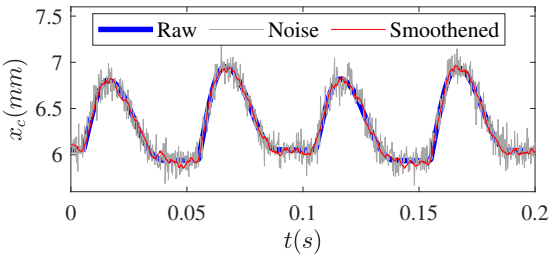

Fig. 4. Example of noise effected and smoothened signals.

Machine learning, especially those involving real-life problems have often required working with huge and lengthy time histories data. Building AI models using such data set can be very costly in terms of computing time, memory and power, and sometimes yield under-performing models. Feature extraction is often used to circumvent this problem and it involves condensing lengthy raw measurements into fewer numerical features manually or automatically. Manual feature extraction often requires expert domain knowledge to identify and extract discriminating features. Automatic feature extraction on the other hand utilises special algorithms to extract features with little or no manual intervention. In this study, manually defined statistical (in time and frequency domains), waveform and nonlinearity features (listed in Table III) were extracted from smoothened x_c signals and used

as inputs into the machine learning models. These features are believed to be indicative of biomechanical difference, however, with complex nonlinear relationship. The schematic layout of the proposed hard-to-visualise early bowel cancer detection is shown in Fig. 5.

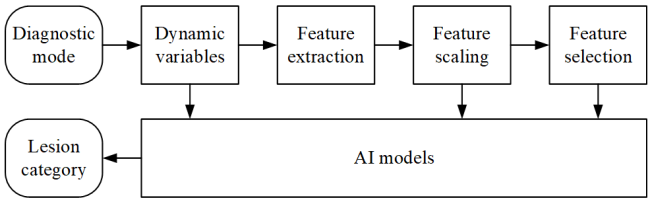

Fig. 5. Schematic layout of the proposed early bowel cancer detection.

Figure 6 shows the nonlinearity between some features and their corresponding stiffness. The features showed higher sensitivity and discrimination at lower stiffness values compared to larger values. The red-broken lines cuts across feature values for $E = 22.8$ kPa using different P_d-values and these are seen to differ despite representing same stiffness. This was the basis for including excitation parameters D, T, P_d, g_1 and the periods of each signal in the network inputs. In all, 47 features were gathered and scaled to have a mean of zero and standard deviation of one based on

$$z = \frac{(x_f - \bar{x}_f)}{\sigma_f}, \tag{5}$$

where z is scaled value, x_f is the original value, $\bar{x}_f$ is the mean and σ_f is the standard deviation of each feature. Figure 7 shows the variation of original 47 features for a particular displacement signal before and after rescaling.

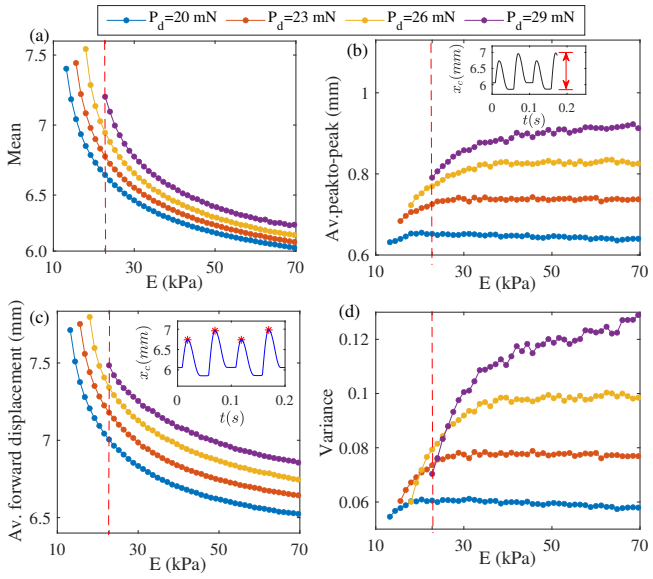

Fig. 6. Comparison of E-values with their corresponding features including (a) mean, (b) average peak-to-peak, (c) average forward displacement and (d) variance. The red-broken lines cut across feature values for E=22.8 kPa for signals of different excitation amplitudes P_d.

IV. Machine Learning Algorithms

In the healthcare sector, machine learning has been applied to surgical robotics and automation [13]–[15] as well as in

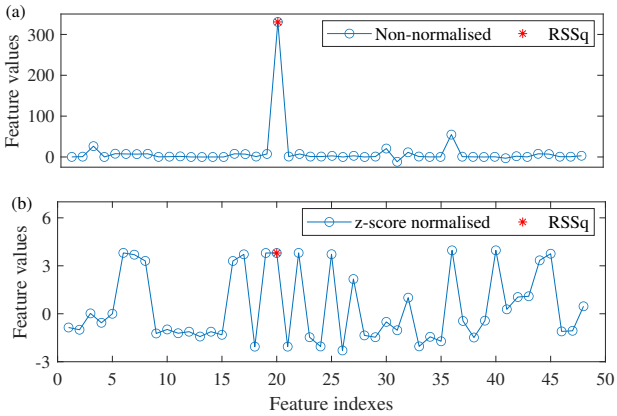

Fig. 7. Variation of defined features for a particular displacement signal (a) before and (b) after scaling.

disease identification and diagnosis [16], [17] using different learning algorithms.

A. Supervised learning algorithms

Supervised learning algorithms are capable of force learning the mapping function between input data and their corresponding targets via examples of input-output pairs. The resulting mapping function is then used to make prediction on similar new input data. In the present study, MLP and SE were used.

1) Multi-Layer Perceptron: MLPs evaluate input information in a single and forward direction using series of interconnected neurons organised in its input, output and hidden layers. Hidden layer can be single or multiple and the neurons of a particular layer interact with those of the following layer via connections of weights w and biases b. MLP learning process involves finding optimal sets of w and b that gives the best output. For input data x_i, $i = 1, 2, ..., N$, the overall network output y^o is given as [18]

$$y^o = f^o\left(\sum_{j=1}^{M} W_j f_h\left(\sum_{i=1}^{N} W_{ij} x_i\right) + b^o\right), \tag{6}$$

where N is the number of input data, M is the number of hidden neurons, x_i is the i^{th} input data, W_{ij} is the weight parameter between the i^{th} input data and j^{th} hidden neuron and W_j is the weight parameter between the j^{th} hidden neuron and the output neuron. Being a classification problem, the activation function f^o is given as a sigmoid function while f_h is a hyperbolic tangent function. The difference between the network's prediction (y^o) and the actual target (y^t) is defined as a cross-entropy error,

$$E_{er} = -\sum_{k=1}^{P}\{y_k^t \ln(y_k^o) + (1 - y_k^t)\ln(1 - y_k^o)\}, \tag{7}$$

where $k = 1, 2, ..., P$, P is the size of outputs. For this work, a two-layer MLP with three hidden neuron each was used.

2) Stacking ensemble classification model: Ensemble learning including bagging, boosting and stacking [19] involves training a set of base learner networks and using

TABLE III

EXTRACTED DYNAMIC SIGNAL FEATURES.

Time domain features	Avg cumulative minimum	Skew factor	**Waveform features**
Mean	Root-mean-square (RMS)	Signal-to-noise ratio (SNR)	Avg forward disp.
Minimum	$\frac{\text{abs(Maximum value)}}{\text{RMS}}$	Total harmonic distortion (THD)	Avg backward disp.
Maximum	Root-sum-of-squares (RSSq)	SNR-to-THD ratio	Avg prominence
Standard deviation	Crest factor	**Frequency domain features**	Peak-to-peak amplitude
Range	Mean absolute value	Mean frequency	Area under curve
Kurtosis	Form factor	Median frequency	**Nonlinearity features**
Variance	Impulse factor	Band power	Lyapunov exponent
Skewness	Mean square root of absolutes	Occupied bandwidth	Correlation dimension
Mean normalised frequency	Kurtosis factor	Power bandwidth	Approximate entropy
Clearance factor	Margin factor	Peak amplitude	
Avg cumulative maximum	Shape factor	Power spectral density	

their prediction outputs as input features for training another network. While bagging and boosting often use copies of same network as base-learners, stacking utilises multiple and heterogeneous networks (see Fig. 8). In this study a SE was developed using support vector machine (SVM) with Gaussian kernel, K-nearest neighbor (KNN), Decision tree (DT), Naïve Bayes (NB), and Random forest (RF). Classification scores rather than the predicted labels of the base learner were obtained as the new input features which were of the same length as the original data. For each base model, a K-fold prediction function ('*kfoldPredict*') as available in MATLAB was used to obtain the five-class classification scores for the training data. This is to avoid creating an overfitted SE. The trained base-learners were also applied on the test data to obtain their classification scores.

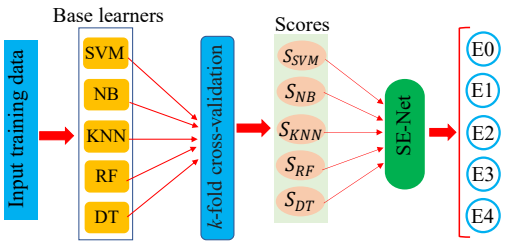

Fig. 8. Concept of the SE classification model.

B. Unsupervised learning algorithms

Unsupervised learning involves learning from input data without making reference to their corresponding targets and it is often used to discover groups of similar examples in the input data. In this study, K-means clustering was adopted to unsupervisedly group the lesions using the extracted features. K-means clustering introduced by MacQueen in 1967 [20] is one of the simplest unsupervised learning algorithms. It aims at partitioning input data into k clusters such that the resulting clusters have high intra-cluster similarity but low inter-cluster similarity.

On initialising, K-means randomly selects n_o number of objects for each cluster from the input data and computes a centroid for them. The remaining data is assigned into the cluster to which they are most similar based on the distance between them and the cluster's centroid. A new centroid is computed for the clusters and the process is iterated. For this study, distance metrics including squared Euclidean distance (SqEucl) and city block (CtyBlk) which respectively use mean and component-wise median as centroids [21] were compared. Due to the medical relevance of this study, clustering results were evaluated by comparing with ground-truth rather than the often used silhouette values.

V. LESION CATEGORISATION

A. Simulation results

For the supervised learning, about 70% and 30% of the data were respectively used for training and testing. Different network models were developed using raw signal data, all extracted feature data and dimensionally reduced feature data. Feature reduction algorithms, including Chi-square tests (fschi2), Minimum Redundancy Maximum Relevance (fsmrmr), Neighborhood Component Analysis (Fsnca), ReliefF (FsRlfF) , Principal Component Analysis (PCA) and Coefficient of Determination ($R^2 > 0.6$), were utilised. Some features were repeatedly selected by two or more algorithms and these include Mean, RMS, Root-sum-of-squares, Mean absolute value, Mean square root of absolute values, Shape factor, Band power and Average forward displacement.

Figure 9 shows the confusion matrices of the base-learners and the resulting SE on test data using Fsschi2 features. The blue diagonal cells indicate the number of correctly classified instances for each class. The blue cell of a particular class represents its true positive while the other blue cells represent its true negative. The brown off-diagonal cells indicate the misclassified instances representing the false positive (in-row) and the false negative (in-column). The overall accuracy of the learners was calculated as

$$\text{Accuracy}(\%) = \frac{\text{TP+TN}}{\text{TP+TN+FP+FN}} \times 100\%, \qquad (8)$$

where TP, TN, FP and FN denote true positive, true negative, false positive and false negative, respectively.

Tables IV and V show the results of the SE and the MLP models on the simulation data. Comparing the base-learners in Table IV, SVM showed better performances as five of its models achieved accuracies greater than 90% on test data. However, the resulting SE outperformed individual base-learners except for the Fscna and R^2 based SVMs. The SE models showed an average accuracy of 91.7% on the

TABLE IV

BASE-LEARNERS AND SE MODELS ACCURACIES (%): SIMULATION.

Feature	Data	SVM	NB	KNN	RF	DT	SE
Raw	Train	99.7	71.5	100	100	98.5	99.9
	Test	93.0	72.2	92.3	92.3	85.6	95.9
All-Fts	Train	99.8	100	98.7	74.5	99.6	99.8
	Test	58.8	75.9	88.1	73.4	91.5	91.4
Fschi2	Train	91.5	42.0	100	85.0	95.5	96.0
	Test	83.8	71.6	79.8	36.4	74.5	88.1
Fsmrmr	Train	96.9	73.3	100	97.7	97.7	98.2
	Test	92.0	85.7	87.0	72.3	87.4	92.6
Fsnca	Train	96.9	73.9	100	95.7	97.5	99.0
	Test	91.2	85.2	84.9	74.9	88.2	89.6
FsRlF	Train	97.4	73.3	100	94.9	97.1	98.8
	Test	93.0	89.4	86.6	73.8	88.1	93.4
PCA	Train	98.8	67.7	100	94.4	95.8	98.9
	Test	81.3	88.6	85.5	67.8	89.3	89.7
R^2	Train	97.1	74.4	100	93.6	96.6	98.8
	Test	94.1	90.1	84.8	74.2	87.9	92.7
Average	Train	97.3	72.0	99.8	92.0	97.3	98.6
	Test	85.9	82.3	86.1	70.6	86.6	91.7
Models $>$ 90%		5	1	1	1	1	5

TABLE V

MLP MODELS ACCURACIES (%): SIMULATION.

Feature	Training	Testing
Raw	95.8	87.5
All-Fts	98.0	97.8
Fscchi2	98.0	97.8
Fscmrmr	98.5	97.5
Fscna	98.5	97.9
ReliefF	98.2	97.7
PCA	98.4	97.0
R^2	98.1	97.8
Average	97.9	96.4

test data with five of them having accuracies greater than 90%. Figure 10 shows the cross-validation performance of Fschi2-based SE model on the test data. It can be observed that the misclassified (red dots) were more concentrated at the boundary for the lower stiffness classes including $E0$, $E1$, $E2$ and $E3$. This might be as a result of the narrow differences between the classes, about $1.2-2.4$ kPa. The occurrence of misclassified samples across the E4 class further establishes the low sensitivity and low discriminative power of extracted features at higher stiffnesses.

Table V shows that the feature-based MLPs significantly outperformed the raw data MLP. Compared to the feature-based SEs, the feature-based MLPs showed better performances with seven of its models yielding accuracies greater than 97% on test data and an average accuracy of 96.4%. However, SE outperformed MLP using the raw signal data as they showed accuracies of 95.9% and 87.5% respectively on the test data. This suggests that SE, combining the powers of multiple base-learners is more suitable for unprocessed raw data, however, at a higher computing cost. The results also showed that further dimensionality reduction via feature selection did not always equate to improved network performance. Some All-Fts models were seen to outperformed some reduced features models.

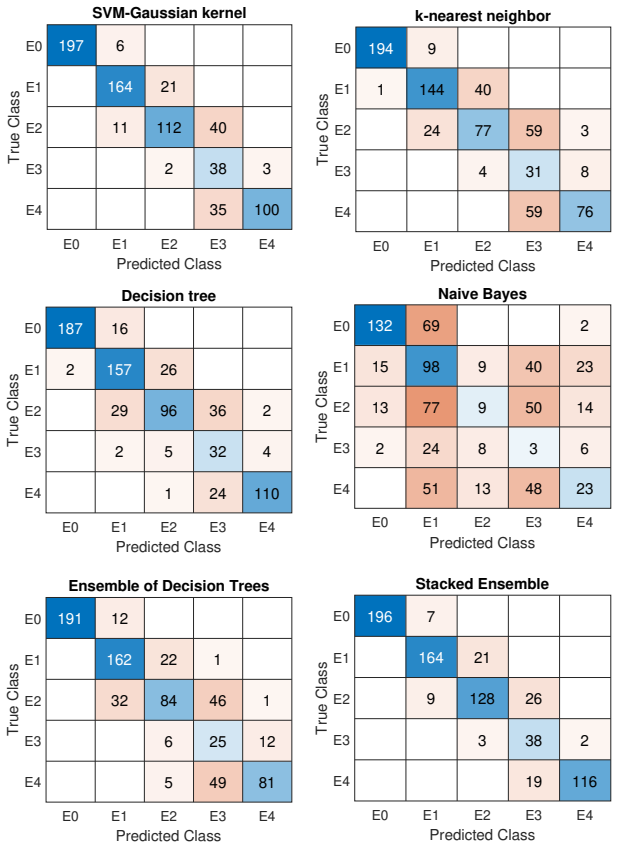

Fig. 9. Confusion matrices of the base-learners and the resulting ensemble network using Fschi2 features.

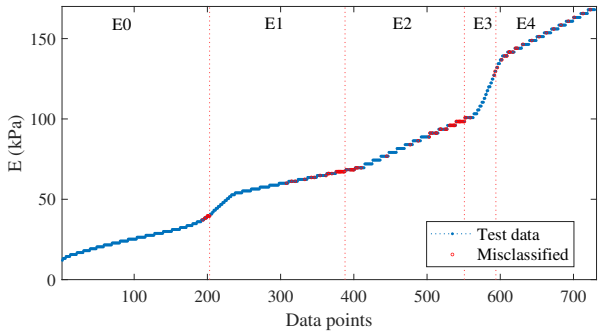

Fig. 10. E-values of the classified out-of-sample test data and misclassified one (circled red) using the Fschi2-based SE.

Attempt to unsupervisedly classify the simulated signals into five lesion classes via K-means clustering as done for supervised learning proved unsuccessful. Same class signals were clustered to belong to two or more different classes, however, a two-class clustering came out successfully (Fig. 11). Samples previously labelled as $E0$ were re-labelled as Category 1 representing benign lesions while classes $E1$, $E2$, $E3$ and $E4$ were re-labelled as Category 2 representing malignant lesions. Results of the K-means clustering are reported in Table VI. SqEucl as a distance metric outperformed CtyBlk with six of its models yielding accuracies greater than 94%. Both metrics, however, achieved greater than 93% accuracies using unprocessed raw signals. Like the supervised models, misclassification

occurred mostly at the boundary of the two classes.

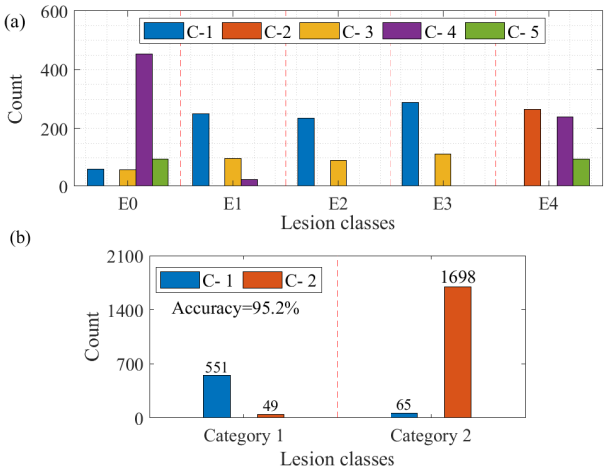

Fig. 11. Unsupervised classification into (a) five classes (b) two classes using K-means clustering.

TABLE VI

K-MEANS CLUSTERING ACCURACIES (%): SIMULATION.

Features	SqEucl	CtyBlk
Raw	94.8	93.4
All	75.5	76.2
Fscchi2	70.2	71.8
Fscmrmr	95.2	89.4
Fscna	95.8	92.8
ReliefF	94.4	88.7
PCA	94.8	88.2
R^2	95.2	87.7
Average	89.5	86.0

B. Experimental validation

For experimental validation, three conical bumps were fabricated from Ecoflex-30, 50 and 80. Ecoflex has in the past been used to represent biological soft tissues [22], [23]. Fabricated bumps were sowed into an artificial intestine of stiffness 25 kPa to create synthetic lesions. Quasi-static test using INSTRON machine revealed the Young's modulus of the synthetic lesions to be E = 56.32 kPa, 84.48 kPa and 168.96 kPa for the Ecoflex-30, 50 and 80 respectively representing $E1$, $E2$ and $E4$ lesion categories. The schematic and laboratory set-up of the experiment are shown in Fig. 12. In all, 977 experimental x_c were obtained by alternating the capsule parameters between D = [0.2, 0.35, 0.5, 0.65, 0.8] and T = [0.05, 0.07, 0.1, 0.2]. The magnetic field at capsule's location was calculated using Biot–Savart's law [24] and this was further used to calculate the excitation amplitude [25], which varied in $P_d \in [40.1, 82.6]$ mN. Savitzky-Golay algorithm was used to smoothen the experimental signals.

Based on low memory requirement, shorter training time and better performance on simulation data, MLP was the only supervised network used in the experimental validation using the three classes experimental data. K-means clustering into two categories was also carried out to validate the unsupervised categorisation. Results of the experimental validation are presented in Table VII. The experimental feature-based MLPs achieved at least 91% accuracies with some achieving 100% and all appending 'NaN' to the none experimentally available classes as shown in Fig. 13. With an average accuracy of 99.6%, K-means clustering using SqEucl outperformed CtyBlk which had average accuracy of 81%. The experimental results also showed that feature selection did not improve the classification.

TABLE VII

EXPERIMENTAL VALIDATION RESULTS.

Features	MLP models (%)		K-means (%)	
	Training	Testing	SqEucl	CtyBlk
Raw	88.3	88.1	100	100
All	100	100	100	100
Fscchi2	99.2	96.2	98.2	54.8
Fscmrmr	100	100	99.4	99.5
Fscna	96.9	95.9	100	100
ReliefF	100	100	100	58.4
PCA	100	99.7	100	35.6
R^2	92.1	91.8	99.4	100
Average	97.1	96.5	99.6	81

VI. CONCLUSIONS

In this study, an AI based dynamic tissue evaluation has been proposed and investigated for the purpose of early bowel cancer detection using a vibration propelled robotic capsule. Using extracted features, supervised MLP and SE network models have been developed and evaluated alongside unsupervised K-means clustering. Extracted features were seen to be more sensitive and discriminative for lower E-values compared to higher E-values. This suggests that the proposed method will be efficient in differentiating between benign lesions and hard-to-visualise early bowel cancers. Based on the implemented feature selection, features that could be of first point of consideration include Mean, RMS, RSSq, Mean absolute value, Mean square root of absolute values, Shape factor, Band power and Average forward displacement. Based on required computing power, training time and resulting accuracies, the MLPs are more preferable for the feature based supervised classification. SE on the other hand is seen to combine the predictive powers of it base-learners to outperform the MLP when using raw and unprocessed signal data, however, at higher computational cost. Most of the resulting SE models outperformed their composite base-learners. Implemented unsupervised classification showed that the lesions are better categorised into two classes representing healthy (benign) and unhealthy (malignant) tissues rather than five classes. K-means clustering using Squared Euclidean distance (SqEucl) as the distance metric outperformed city block (CtyBlk). Further analysis of the prediction results showed that most of the misclassification occurred at the boundary of the classes.

The overall performance analysis of the proposed methodology indicates its huge potential to improve bowel cancer treatment and survival via early detection. As future works, a threshold difference needs to be established for the E-values of benign lesions and early bowel cancer lesions. Also, the current study requires an in-vivo testing.

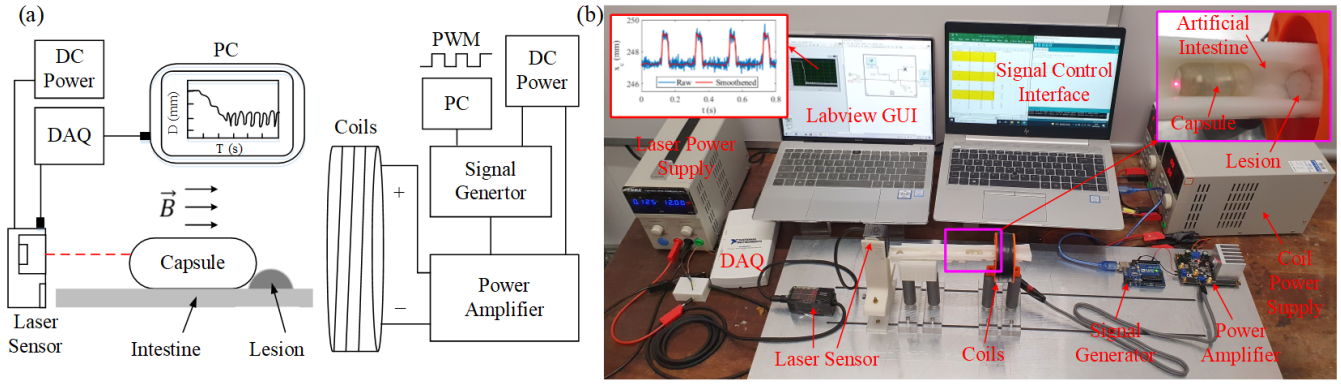

Fig. 12. (a) Schematic and (b) photograph of the experimental setup. The T-shaped magnet inside the capsule prototype was excited through an on-off electromagnetic field $\vec{B}$ and the helical spring to generate forward and backward impact motion, leading to the locomotion of the prototype. The on-off external excitation was generated using a signal generator producing a pulse width modulation (PWM) signal via a power amplifier, and the amplifier can control the voltage applied to the coils by adjusting a DC power supply. The prototype was put on a piece of cut-open synthetic intestine supported by a halved black plastic tube, which was placed along the axis centre of the coils. Three conical bumps made by Ecoflex-30, 50 and 80 were sowed into the artificial intestine to create synthetic lesions representing $E1$, $E2$ and $E4$ lesion categories, respectively. On the left of the experimental setup, a laser sensor was used to record the displacement of the capsule, and recorded data were smoothed and analysed for lesion classification.

Fig. 13. Confusion matrix of the All-features based MLP.

REFERENCES

[1] J. Ferlay, M. Ervik, F. Lam, M. Colombet, L. Mery, M. Piñeros, A. Znaor, I. Soerjomataram, and F. Bray. Global cancer observatory: Cancer today. [Online]. Available: https://gco.iarc.fr/today

[2] N. Bannister and J. Broggio. Cancer survival by stage at diagnosis for England (experimental statistics): adults diagnosed 2012, 2013 and 2014 and followed up to 2015. [Online]. Available: https://www.gov.uk/search/research-and-statistics

[3] D. Myers and D. Paul. Colon polyps and your cancer risk. [Online]. Available: https://www.verywellhealth.com/colon-polyps-and-cancer-risk-797579

[4] E. Dekker, P. J. Tanis, J. L. A. Vleugels, P. M. Kasi, and M. B. Wallace, "Colorectal cancer," *The Lancet*, vol. 394, pp. 1467–1480, 2019.

[5] Cancer Research UK. Capsule endoscopy. [Online]. Available: https://www.cancerresearchuk.org/about-cancer/cancer-in-general/tests/capsule-endoscopy

[6] F. Gong, P. Swain, and T. Mills, "Wireless endoscopy," *Gastrointestinal Endoscopy*, vol. 51, no. 6, pp. 725–729, 2000.

[7] W. H. Kim, Y. J. Cho, J. Y. Park, P. K. Min, J. K. Kang, and I. S. Park, "Factors affecting insertion time and patient discomfort during colonoscopy," *Gastrointestinal Endoscopy*, vol. 52, pp. 600–605, 2000.

[8] E. Brauchle, J. Kasper, R. Daum, N. Schierbaum, C. Falch, A. Kirschniak, T. E. Schäffer, and K. Schenke-Layland, "Biomechanical and biomolecular characterization of extracellular matrix structures in human colon carcinomas," *Matrix Biology*, vol. 68, pp. 180–193, 2018.

[9] P. Deptula, D. Lysik, K. Pogoda, M. Cieśluk, A. Namiot, J. Mystkowska, G. Król, S. Gluszek, P. Janmey, and R. Bucki, "Tissue rheology as a possible complementary procedure to advance histological diagnosis of colon cancer," *ACS Biomaterials Science & Engineering*, vol. 6, pp. 5620–5631, 2020.

[10] M. Brás, S. Sousa, F. Carneiro, M. Radmacher, and P. Granja, "Mechanobiology of colorectal cancer," *Cancers*, vol. 14, p. 1945, 2022.

[11] Y. Yan, B. Zhang, Y. Liu, and S. Prasad, "Dynamics of a vibro-impact self-propelled capsule encountering a circular fold in the small intestine," *Meccanica*, pp. 1–22, 2022.

[12] B. Guo, E. Ley, J. Tian, J. Zhang, Y. Liu, and S. Prasad, "Experimental and numerical studies of intestinal frictions for propulsive force optimisation of a vibro-impact capsule system," *Nonlinear Dynamics*, vol. 101, pp. 65–83, 2020.

[13] A. Attanasio, B. Scaglioni, M. Leonetti, A. F. Frangi, W. Cross, C. S. Biyani, and P. Valdastri, "Autonomous tissue retraction in robotic assisted minimally invasive surgery–a feasibility study," *IEEE Robotics and Automation Letters*, vol. 5, pp. 6528–6535, 2020.

[14] J. W. Martin, B. Scaglioni, J. C. Norton, V. Subramanian, A. Arezzo, K. L. Obstein, and P. Valdastri, "Enabling the future of colonoscopy with intelligent and autonomous magnetic manipulation," *Nature Machine Intelligence*, vol. 2, pp. 595–606, 2020.

[15] P. Lloyd, A. K. Hoshiar, T. da Veiga, A. Attanasio, N. Marahrens, J. H. Chandler, and P. Valdastri, "A learnt approach for the design of magnetically actuated shape forming soft tentacle robots," *IEEE Robotics and Automation Letters*, vol. 5, pp. 3937–3944, 2020.

[16] S. Yang, C. Lemke, B. F. Cox, I. P. Newton, I. Näthke, and S. Cochran, "A learning-based microultrasound system for the detection of inflammation of the gastrointestinal tract," *IEEE Transactions on Medical Imaging*, vol. 40, pp. 38–47, 2020.

[17] L. Wang, Y. Sun, Q. Li, T. Liu, and J. Yi, "Two shank-mounted imus-based gait analysis and classification for neurological disease patients," *IEEE Robotics and Automation Letters*, vol. 5, pp. 1970–1976, 2020.

[18] C. M. Bishop *et al.*, *Neural networks for pattern recognition*. Oxford University Press, 1995.

[19] D. H. Wolpert, "Stacked generalization," *Neural Networks*, vol. 5, pp. 241–259, 1992.

[20] J.-G. Sun, J. Liu, and L.-Y. Zhao, "Clustering algorithms research," *Journal of Software*, vol. 19, pp. 48–61, 2008.

[21] Mathworks. K-means clustering. [Online]. Available: https://uk.mathworks.com/help/stats/kmeans.html

[22] J. L. Sparks, N. A. Vavalle, K. E. Kasting, B. Long, M. L. Tanaka, P. A. Sanger, K. Schnell, and T. A. Conner-Kerr, "Use of silicone materials to simulate tissue biomechanics as related to deep tissue injury," *Advances in Skin & Wound Care*, vol. 28, pp. 59–68, 2015.

[23] H. Xie, J. Song, Y. Zhong, C. Gu, and K.-S. Choi, "Constrained finite element method for runtime modeling of soft tissue deformation," *Applied Mathematical Modelling*, vol. 109, pp. 599–612, 2022.

[24] B. Gellert, "Turbogenerators in gas turbine systems," in *Modern Gas Turbine Systems*. Elsevier, 2013, pp. 247–326.

[25] S. Schuerle, S. Erni, M. Flink, B. Kratochvil, and B. Nelson, "Three-dimensional magnetic manipulation of micro-and nanostructures for applications in life sciences," *IEEE Transactions on Magnetics*, vol. 49, pp. 321–330, 2012.